Int J Fract (2009) 160:31–41
DOI 10.1007/s10704-009-9400-1

ORIGINAL PAPER

Failure of plain concrete beam at impact load: 3D finite element analysis

V. Travaš · J. Ožbolt · I. Kožar

Received: 27 February 2009 / Accepted: 10 September 2009 / Published online: 26 September 2009

Abstract In the paper, the results of numerical failure analysis of plain concrete beams loaded by impact three-point bending load are presented and discussed. The theoretical framework for the numerical analysis is continuum mechanics and irreversible thermodynamics. The spatial discretization is performed by the finite element method using update Lagrange formulation. Green–Lagrange stain tensor is used as a strain measure. To account for cracking and damage of concrete, the beam is modeled by the rate sensitive microplane model with the use of the so-called co-rotational stress tensor. Damage and cracking phenomena are modeled within the concept of smeared cracks. To assure objectivity of the analysis with respect to the size of the finite elements, crack band method is used. The contact-impact analysis is based on the mechanical interaction between two bodies—concrete beam (master) and dropping hammer (slave) falling on the mid span of the beam. The contact constrains are satisfied by Lagrange multiplier method, which is adapted for the explicit time integration scheme. To investigate the influence of loading rate on the failure mode of the beam parametric study is carried out. The numerical results are evaluated, discussed and compared with test results known from the literature. It is shown that the beam resistance and failure mode strongly depend on loading rate. For lower loading rates beam fails in bending (mode-I fracture). However, with increasing loading rate there is a transition of the failure mechanism from bending to shear. The results are in good agreement with theoretical and experimental results known from the literature.

Keywords Rate sensitivity · Plain concrete beam · Fracture · Contact-impact problem · Finite elements · Microplane model

V. Travaš · I. Kožar
Faculty of Civil Engineering, University of Rijeka,
51000 Rijeka, Croatia

V. Travaš
e-mail: vanja.travas@gradri.hr

I. Kožar
e-mail: ivica.kozar@gradri.hr

J. Ožbolt (✉)
Institute of Construction Materials, University of Stuttgart,
70550 Stuttgart, Germany
e-mail: ozbolt@iwb.uni-stuttgart.de

1 Introduction

The results of theoretical and experimental investigations show that loading rate significantly influences the response of structures made of quasi-brittle materials, such as concrete. Comparing concrete response at static or quasi-static loading with the response for high loading rate (impact), it can be seen that the concrete nominal strength increases with increase of loading rate. Moreover, it is known that the failure mechanism also depends on loading rate. Principally, the structural response depends on loading rate through three different effects: (1) through creep of the bulk

material between the cracks, (2) through the rate dependency of the growing micro-cracks, and (3) through the effect of structural inertia forces, which can significantly influence the state of stresses and strains at the material level. In general, each of the mentioned influences is always present. However, depending on the material type and loading rate, the first, the second or the third effect may dominate. For quasi-brittle materials, such as concrete, which exhibit cracking and damage phenomena, the first effect is important only for relatively low loading rates (creep–fracture interaction), the second for intermediate loading rates and the last one is dominant in case of relatively high loading rates (impact).

Various theoretical and experimental studies were in the past conducted in order to investigate the effect of loading rate on the response of concrete structures (Dilger et al. 1978; Reinhardt 1982; Curbach 1987; Comite Euro-International Du Beton 1988; Bažant and Gettu 1992; Weerheijm 1992; Ožbolt and Reinhardt 2001, 2005a,b; Ožbolt et al. 2006; Saatci and Vecchio 2009). In most of the studies different constitutive relations, similar to the spring–dashpot models of visco-elasticity, were employed. Some of the models cover only a limited range of loading rates whereas the other are more general and applicable over many orders of magnitude of loading rate. However, apart from the influence of the loading rate on the structural response, an additional problem at high impact mechanics is rather complex energy transfer mechanism over the contact surfaces between the bodies under collision. Therefore, impact loading cannot be simply viewed only as a problem of strain rate. As discussed by Bentur et al (1987) and Banthia et al. (1987), in an experiment it is difficult to satisfy the energy balance through the measuring of mechanical energies. In contrary to the experimental investigations, assuming isothermal conditions, in numerical analysis the transformation of impact kinetic energy into other mechanical energies can be easily calculated. Due to the fact that the failure process in concrete occurs in a very short period of time, numerical study is useful and necessary for better understanding of damage phenomena at impact loading.

Currently there are only a limited number of numerical and experimental studies in which the failure mode is investigated as a function of loading rate (Sukontasukkul and Mindess 2003; Ožbolt and Reinhardt 2005a,b; Saatci and Vecchio 2009). In the present numerical study, a rate dependent microplane material model for concrete is used. The rate dependent microplena model for concrete was originally proposed by Bažant et al. (2000b). The model is based on the rate process theory (Krausz and Krausz 1988) of bond ruptures, which is coupled with the microplane model for concrete (Ožbolt et al. 2001, 2006). The aim of the study is to check whether the numerical model is able to realistically predict the rate dependent failure mechanism of plain concrete beam and to see the influence of impact velocity on the response of plain concrete beam. The numerical experiment is conducted by 3D finite element simulation of the free fall of hammer, where the dropped hammer falls from different heights. The contact force between the dropped hammer and the concrete beam is unknown, therefore, the mechanical interaction between the beam (master) and the hammer (slave) is simulated. The investigated range of impact velocities is such that the strain rates are very high but still smaller than the strain rates at which the dropping hammer would cause extreme local concrete damage (crushing) of the impact zone. The paper consists of two parts. In the first part theoretical and numerical aspects that are related to the numerical solution of the contact-impact problem are discussed. In the second part, the numerical results are presented, evaluated and discussed.

2 Formulation of the contact-impact problem

2.1 General

The problem is formulated in the framework of continuum mechanics assuming the validity of irreversible thermodynamics (isothermal conditions). The numerical spatial discretization is performed by the linear tetrahedral finite elements (Zienkiewicz et al. 2005). In the incremental transient finite element analysis, the so-called update Lagrange formulation of the governing differential equations is employed, i.e., the equilibrium is required on current (deformed) geometry. Green–Lagrange finite strain tensor is used as a strain measure (Belytschko et al. 2001; Crisfield 1991). As a constitutive law, the rate dependent microplane model for concrete is employed together with the so-called co-rotational stress tensor (Bažant et al. 2000a; Ožbolt et al. 2006).

2.2 Strong and weak form of the governing differential equations

Let's consider a system of bodies $\mathcal{B}^\kappa$, with κ denoting each of them. Adopting index notation, for the entire deformation history the balance of linear momentum reads:

$$\sigma^\kappa_{ij,j} + \rho^\kappa f^\kappa_i = \rho^\kappa \ddot{u}^\kappa_i \quad \text{for } i, j = 1, 2, 3 \tag{1}$$

where $\sigma_{ij,j}$ is divergence of the true Cauchy stress tensor, u_i is displacement with dot indicating its time derivatives. If the boundary conditions between the starting time t_0 (initial time) and current time t are known, the trajectory of each point in the deformable continuum is uniquely defined. The Dirichlet displacement boundary conditions on surface Γ^κ_u are:

$$u^\kappa_i = u^\kappa_{i,0} \quad \text{on } \Gamma^\kappa_u \tag{2}$$

in which $u^\kappa_{i,0}$is known displacement field. Denoting the boundary surface unit outward normal vector with n^κ_i, the additional Neumann traction boundary conditions $t^\kappa_{i,0}$ on the boundary Γ^κ_t reads:

$$\sigma^\kappa_{ij} n^\kappa_i = t^\kappa_{i,0} \quad \text{on } \Gamma^\kappa_t \tag{3}$$

To solve the problem of contact between two or more bodies in the framework of continuum mechanics, there are two basic additional restrictions on the displacement and traction field over the contact surfaces Γ^κ_C. From the fact that two material points cannot occupy the same space at the same time, the penetration of one into another body is not possible. Let's assume that the negative gap value g^κ_i indicates the magnitude of the non-physical penetration, then the first condition, condition of impenetrability, states that no penetration is allowed:

$$g^\kappa_i \geq 0\,; \quad g^\kappa_i = \begin{cases} > 0 & \text{nocontact} \\ 0 & \text{contact} \\ < 0 & \text{penetration} \end{cases} \tag{4}$$

The second condition assures the compressive character of the normal traction acting on the contact surface Γ^κ_C. This is so called intensility condition:

$$t^\kappa_i \leq 0 \quad \text{on } \Gamma^\kappa_C \tag{5}$$

Finally, combination of impenetrability condition (4) with the intensility condition (5) yields to the so-called complementarity condition:

$$g^k_i t^k_i = 0 \tag{6}$$

Under the assumption that the deformation of bodies does not cause mechanical interaction (contact), the weak form of dynamic equilibrium equation for body $\mathcal{B}^\kappa$ (1) can be obtained by applying the Hamilton's variational principle of least action:

$$\int_{\Omega^\kappa} \rho^\kappa \ddot{u}^\kappa_i \, \delta u_i \, d\Omega^\kappa + \int_{\Omega^\kappa} \sigma^\kappa_{ij,j} \delta u_i \, d\Omega^\kappa - \int_{\Omega^\kappa} \rho^\kappa f^\kappa_i \delta u_i \, d\Omega^\kappa - \int_{\Gamma^\kappa} t^\kappa_i \delta u_i \, d\Gamma^\kappa = 0 \tag{7}$$

Since in general there are more than two bodies, they can mechanically interact between each other. Consequently, the contact surfaces are time dependent. To account for this scenario, the displacement field has to be restricted by excluding those displacements that cause non-physical penetration. From the various strategies available for the enforcement of contact condition (Wriggers 2002), in the present formulation the Lagrange multiplier method is used (Belytschko et al. 2001; Wriggers 2002). From the mechanical point of view, Lagrange multiplier λ represents force that is needed for the separation of bodies after a non-physical penetration is detected (4). The contact situation can be energetically described by introducing the artificial "parasite" contact energy Π^k_C stored on the contact interface (surface) Γ^κ_C. The contact energy is defined by the work of Lagrange multipliers on not-allowable gaps g^κ_n. Assuming that the frictional energy on the contact surface is fully dissipative, only normal contact forces λ^κ_n contribute to contact energy. The entire contact energy is calculated as:

$$\Pi^\kappa_C = \int_{\Gamma^\kappa_C} \lambda^\kappa_n \, g^\kappa_n \, d\,\Gamma^\kappa_C \tag{8}$$

The variation and minimization of (8), that is a weak form of (4), and its combination with (7) yields to the weak form of dynamic equilibrium equation for bodies $\mathcal{B}^\kappa$ in contact:

$$\int_{\Omega^\kappa} \rho^\kappa \ddot{u}^\kappa_i \delta u_i d\Omega^\kappa + \int_{\Omega^\kappa} \sigma^\kappa_{ij} \delta u_{ij} d\Omega^\kappa - \int_{\Omega^\kappa} \rho^\kappa f^\kappa_i \delta u_i d\Omega^\kappa - \int_{\Gamma^\kappa} t^\kappa_i \delta u_i d\Gamma^\kappa + \partial\Pi^\kappa_C = 0 \tag{9}$$

$$\text{with: } \partial\Pi^\kappa_C = \int_{\Gamma^\kappa_C} \lambda^\kappa_n \delta g^\kappa_n d\Gamma^\kappa_C + \int_{\Gamma^\kappa_C} \delta\lambda^\kappa_n g^\kappa_n d\Gamma^\kappa_C$$

2.3 Finite element discretization and numerical algorithm

The numerical approximation of (9) is performed by finite elements. Following the standard finite element formulation and accounting for constrains on contact surfaces of finite elements, the discrete form of (9) becomes (Voight notation):

$$\mathbf{M\ddot{u}} + \mathbf{C\dot{u}} + \mathbf{Ku} + \mathbf{G}^{\mathbf{T}}\lambda = \mathbf{R} \tag{10a}$$

$$\mathbf{G\{u + X\}} = \mathbf{0} \tag{10b}$$

where $\mathbf{M}$ is the global diagonal mass matrix, $\mathbf{K}$ the global secant stiffness matrix and $\mathbf{R}$ the known load vector. The influence of vicious damping is introduced through damping matrix $\mathbf{C}$ obtained by linear combination of matrix $\mathbf{M}$ and $\mathbf{K}$. Note, that the product $\mathbf{Ku}$ represents internal nodal forces due to deformation of bodies. Matrix $\mathbf{G}$ is the element contact displacement constraint matrix and $\boldsymbol{\lambda}$ is the vector of unknown Lagrange multipliers. The last term on the left hand side of (10a) is the discrete form of contact forces and (10b) is the discrete form of the contact displacement constrains, where $\mathbf{X}$ is the material coordinate vector. Note, that by definition the contact element consists of one contractor node (slave node), which comes into contact with the mesh of target surface (master surface) defined by three nodes on one free finite element boundary plane (triangle plane).

The system of differential algebraic equation (10) is solved using the explicit time integration scheme and update Lagrange formulation. In the solution strategy the multi-step central difference method (Wriggers 2002) is adopted. The equation of motion (10a) for the time step t_{n} and displacement constrains (10b), which are calculated at the time step $t_{\mathrm{n+1}}$ and related to contact forces obtained at time t_{n}, can be written as:

$$\mathbf{M\ddot{u}}_{\mathrm{n}} + \mathbf{C\dot{u}}_{\mathrm{n}} + \mathbf{Ku}_{\mathrm{n}} + \mathbf{G}^{\mathbf{T}}_{\mathrm{n+1}}\boldsymbol{\lambda}_{\mathrm{n}} = \mathbf{R}_{\mathrm{n}} \tag{11a}$$

$$\mathbf{G}_{\mathrm{n+1}}\{\mathbf{u}_{\mathrm{n+1}} + \mathbf{X}\} = \mathbf{0} \tag{11b}$$

$$\text{with}: \dot{\mathbf{u}}_{\mathrm{n}} = \frac{1}{2\Delta t}\{\mathbf{u}_{\mathrm{n+1}} - \mathbf{u}_{\mathrm{n-1}}\}$$

$$\ddot{\mathbf{u}}_{\mathrm{n}} = \frac{1}{\Delta t^2}\left\{\mathbf{u}_{\mathrm{n+1}} - 2\mathbf{u}_{\mathrm{n}} + \mathbf{u}_{\mathrm{n+1}}\right\} \tag{11c}$$

In the update Lagrange formulation equilibrium is required on the current configuration $\mathbf{x}_{\mathrm{n}}$ that is continuously updated as:

$$\mathbf{x}_{\mathrm{n+1}} = \mathbf{X} + \mathbf{u}_{\mathrm{n+1}} \tag{12}$$

in which $\mathbf{x}_{\mathrm{n+1}}$ is the coordinate vector of the current mesh configuration calculated by adding displacement vector $\mathbf{u}_{\mathrm{n+1}}$ to the vector of material coordinates $\mathbf{X}$.

The unknown displacement $\mathbf{u}_{\mathrm{n+1}}$ at the end of the time interval Δt can be calculated in four steps. Neglecting for a moment the influence of the contact in (11a), the computation starts with the contact predictor phase where the nodal displacement increments are calculated using standard explicit update:

$$\mathbf{u}^{D}_{\mathrm{n+1}} = \left[\mathbf{M} + \frac{\Delta t}{2}\mathbf{C}\right]^{-1} \left\{\Delta t^2\{\mathbf{K}\,\mathbf{u}_{\mathrm{n}} - \mathbf{R}_{\mathrm{n}}\} + \frac{\Delta t}{2}\mathbf{C}\,\mathbf{u}_{\mathrm{n-1}} + \mathbf{M}\,\{2\mathbf{u}_{\mathrm{n}} - \mathbf{u}_{\mathrm{n-1}}\}\right\} \tag{13}$$

The computation proceeds with activating the so-called global contact detection algorithm, where the search over the possible non-physical penetrations of the boundary mesh nodes is tested (Hutter and Fuhrmann 2007). For those contractor nodes that violate the contact constraint equation (11b) and penetrate into a mesh domain, an additional local detection strategy is activated. As a result, data needed for calculation of constraint matrix $\mathbf{G}_{\mathrm{n+1}}$ are obtained. The contact forces, represented by the Lagrange multiplier $\boldsymbol{\lambda}_{\mathrm{n}}$, are than calculated for each contact element as:

$$\lambda_{\mathrm{n}} = \left[\Delta t^2\,\mathbf{G}_{\mathrm{n+1}}\mathbf{M}^{-1}\,\mathbf{G}^{\mathbf{T}}_{\mathrm{n+1}}\right]^{-1}\mathbf{G}_{\mathrm{n+1}} \left\{\mathbf{u}^{D}_{\mathrm{n+1}} + \mathbf{X} - \mathbf{u}_{\mathrm{n}}\right\} \tag{14}$$

To remove the penetrated nodes from contact, in the contact correction phase, an incremental contact displacements $\mathbf{u}^{C}_{\mathrm{n+1}}$ are calculated by distributing the contact forces from (14) to each contact element node using the displacement constraint matrix $\mathbf{G}_{\mathrm{n+1}}$:

$$\mathbf{u}^{C}_{\mathrm{n+1}} = -\Delta t^2\mathbf{M}^{-1}\,\mathbf{G}^{T}_{\mathrm{n+1}}\,\lambda_{\mathrm{n}} \tag{15}$$

At the end of the time interval Δt, the total nodal displacements $\mathbf{u}_{n+1}$are calculated as:

$$\mathbf{u}_{\mathrm{n+1}} = \mathbf{u}^{D}_{\mathrm{n+1}} + \mathbf{u}^{C}_{\mathrm{n+1}} \tag{16}$$

Due to the fact that the mechanical interaction is nonlinear, (13, 14, 15) are solved using Gauss-Seidel iterative algorithm (Carpenter et al. 1991). To avoid numerical instability of the explicit algorithm, the time increment Δt must be smaller than the critical time increment Δt_{cr}. The critical time increment $\Delta t^{e}_{\mathrm{cr}}$ for the finite element e, is calculated as:

$$\Delta t^e_{\mathrm{cr}} = \frac{L^e_{\min}}{\sqrt{E^\kappa/\rho^\kappa}}; \quad e = 1, \ldots, n_e; \quad \Delta t < \min\left(\Delta t^e_{\mathrm{cr}}\right) \tag{17}$$

where $L^e_{\min}$ is the minimal length of the finite element edges, E^e and ρ^e are Young's modulus and density, respectively.

3 Rate dependent microplane model for concrete

In the microplane model the material is characterized by the relation between stress and strain components on planes of various orientations. These planes may be imagined to represent damage planes or weak planes in the microstructure, such as those that exist at the contact between aggregate and cement matrix. In contrast to phenomenological models for concrete, which are based on tensor invariants, in the microplane model the tensorial invariance restrictions need not be directly enforced. Superimposing in a suitable manner the responses from all the microplanes automatically satisfies them.

The used microplane model (Ožbolt et al. 2001) is based on the so-called relaxed kinematic constraint concept. It is a modification of the M2 microplane model proposed by Bažant and Prat (1988). Each microplane is defined by its unit normal vector components n_i (see Fig. 1). Microplane strains are assumed to be the projections of macroscopic strain tensor ε_{ij} (kinematic constraint). On each microplane considered are normal and shear stress-strain components $(\sigma_N, \sigma_{Tr}, \varepsilon_N, \varepsilon_{Tr})$. To realistically model concrete, the normal microplane stress and strain components have to be decomposed into volumetric and deviatoric parts $(\sigma_N = \sigma_V + \sigma_D, \varepsilon_N = \varepsilon_V + \varepsilon_D)$. Based on the micro–macro work conjugancy of volumetric–deviatoric split and using in advance defined microplane stress–strain constitutive laws, the macroscopic stress tensor is calculated as an integral over all possible, in advance defined, microplane orientations:

$$\sigma_{ij} = \sigma_V \delta_{ij} + \frac{3}{2\pi}\int_S \sigma_D \left(n_i n_j - \frac{\delta_{ij}}{3}\right) dS + \frac{3}{2\pi}\int_S \frac{\sigma_{Tr}}{2}(n_i \delta_{rj} + n_j \delta_{rj})\, dS \tag{18}$$

where S denotes the surface of the unit radius sphere and δ_{ij} is Kronecker delta. The integration is performed

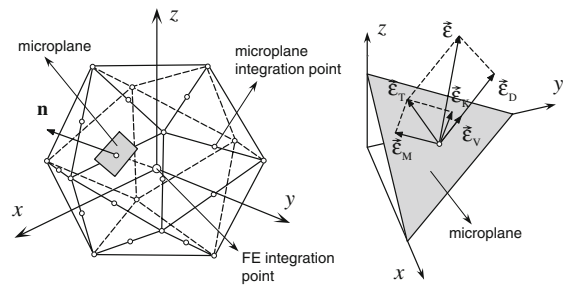

Fig. 1 Decomposition of the macroscopic strain vector into microplane strain components—normal (volumetric and deviatoric) and shear

by numerical integration using 21 integration points (symmetric part of the sphere, see Fig. 1).

In general case displacements can be large and strains finite, e.g., penetration of a nail into a concrete block. For such a case, as a strain measure Green-Lagrange finite strain tensor is used. Moreover, since the response of concrete is path dependent, the co-rotational stress tensor should be employed (Bažant et al. 2000a). This means that microplane directions are not fixed, they rotate with the rotation of the point of continuum (integration point). Note, however, that in the present numerical study strains and displacements are small. Consequently, the co-rotational stress tensor coincide with the true (Cauchy) stress tensor. Detailed discussion of the features and various aspects related to the finite strain formulation of the microplane model are beyond the scope of the present paper. For more detail refer to Bažant et al. (2000a) and Ožbolt et al. (2001).

At the constitutive level the rate dependency consists of two parts: (1) the rate dependency related to the formation of the microcracks, and (2) the rate dependency due to the creep of concrete between the microcracks. The influence of inertia forces on the rate effect is not a part of the constitutive law, however, this effect is automatically accounted for in dynamic analysis in which the constitutive law interacts with inertia forces. The discussion related to the influence of creep is out of the scope of the paper. Based on the activation energy theory (Krausz and Krausz 1988), the influence of strain rate on the rate insensitive microplane stress $\sigma^0_m(\varepsilon_m)$, where m indicates microplane stress–strain components V, D and T_r, can be written as (Bažant et al. 2000b; Ožbolt et al. 2006):

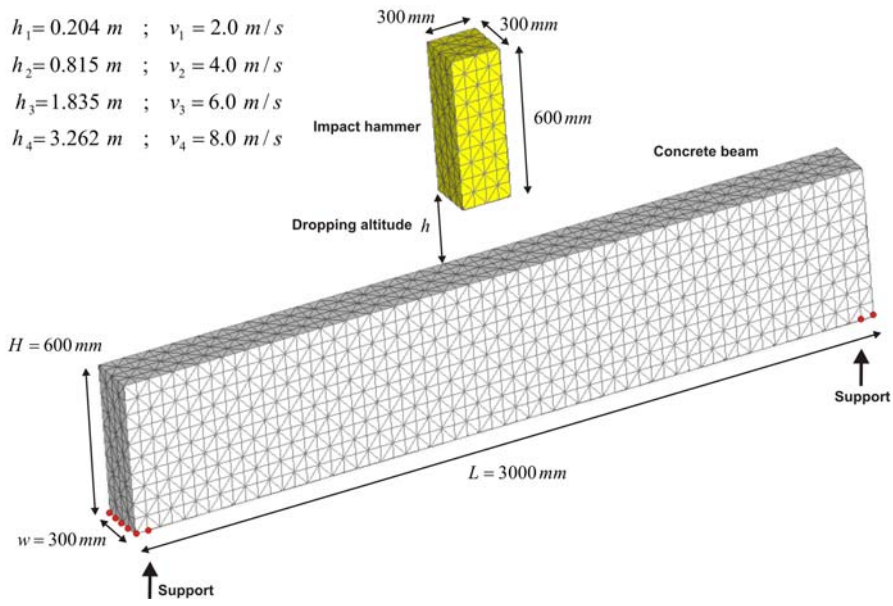

Fig. 2 Geometry of the investigated plain concrete beam

$$\sigma_m(\varepsilon_m) = \sigma_m(\varepsilon_m)\left[1 + c_2 \ln\left(\frac{2\dot{\gamma}}{c_1}\right)\right]$$

$$\text{with: } \dot{\gamma} = \sqrt{\frac{1}{2}\dot{\varepsilon}_{ij}\dot{\varepsilon}_{ij}}\ \ c_1 = \frac{c_0}{s_{\text{cr}}} \tag{19}$$

where c_0 and c_2 are material constants, which have to be calibrated by fit of test data. Note, that because for $\dot{\gamma}^2 \gg 1$ $a\sinh\dot{\gamma} \approx \ln(2\dot{\gamma})$, instead of asinh, which is exact solution according to energy activation theory, in (19) is used logarithmic function. The calibration of the constitutive law was carried out for moderate loading rates for which inertia forces have not much influence on the rate dependent response of concrete, i.e., only the rate of crack growth controls the response. For more detail see Ožbolt et al. (2006).

4 Numerical analysis of plain concrete beam under impact load

Experimental tests on plain and reinforced concrete beams (Comite Euro-International Du Beton 1988; Sukontasukkul and Mindess 2003) loaded by three-point bending showed that resistance and brittleness of beams increase with the increase in loading rate. Furthermore, it was shown that for relatively low loading rate the failure is due to bending (mode-I fracture). With increase in loading rate there is a transition of the failure mode from bending to shear. The main difficulty in the experiments with high loading rates is the measurement of the beam response. This is due to the fact that fracture takes place in a rather short period of time. The numerical analysis is performed because of two reasons: (1) to investigate whether the numerical model is able to reproduce the test results qualitatively correct and (2) to investigate in more detail the response of concrete beam, e.g., cracking rate, distribution of energies, transition of failure mode etc., for different loading rates. The numerical study is carried out using the above discussed numerical approach. Cracking and damage phenomena in concrete are modeled using the concept of smeared cracks. To obtain mesh objective results crack band method is employed (Bažant and Oh 1983; Ožbolt and Bažant 1996).

The plain concrete beam is loaded by impact hammer at the mid-span (see Fig. 2). The dimensions of the beam are: length–height–width = 3000 × 600 × 300 mm. The mechanical properties of concrete are: Young's modulus $E_c = 30{,}000$ N/mm^2, Poisson's ratio $\nu = 0.18$, uni-axial compressive strength $f_c = 45.0$ N/mm^2, tensile strength $f_t = 2.70$ N/mm^2, fracture energy $G_F = 0.10$ N/mm, and concrete mass density $\rho_c = 2{,}300$ kg/m^3. The load is applied through the kinetic energy of dropping hammer. The length of the hammer is 600 mm and the cross-section area is 300 × 300 mm. The behavior of hammer is

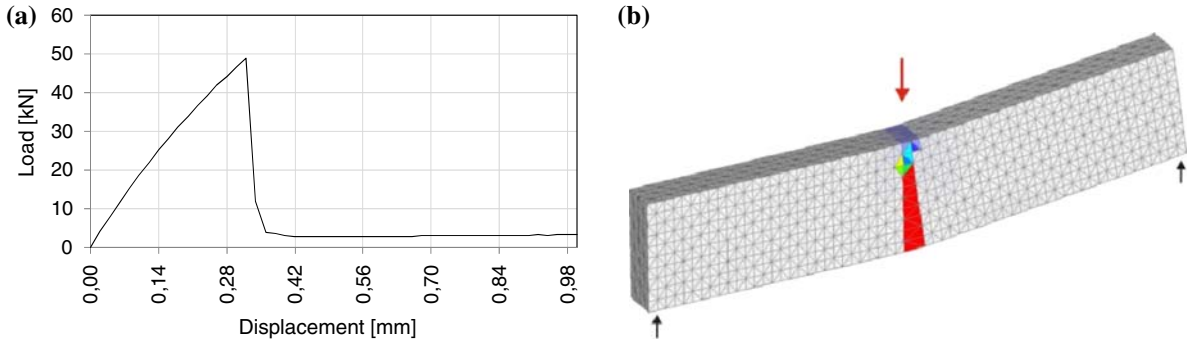

Fig. 3 Quasi-static analysis **a** Load-displacement curve. **b** Failure mode

assumed to be linear elastic with Young's modulus of 20,0000 N/mm^2 and mass density of 8,000 kg/m^3. On the beam-hammer contact surface, the frictional coefficient $\mu = 0.5$ is assumed. The numerical analysis is performed for quasi-static loading and for impact loading velocities of 2, 4, 6 and 8 m/s.

The results of the quasi-static analysis are shown in Fig. 3. Plotted are mid-span load-displacement curve and failure mode. As expected, the failure is of mode-I type (bending). The crack (red zone) is plotted in terms of maximal principal strains. It is assumed the critical crack opening $w_{cr} = 0.2$ mm what corresponds to the critical strain of $\varepsilon_{cr} = w_{cr}/h_e = 0.0033$, with h_e equal to average element size (60 mm).

Figure 4 shows predicted failure modes for impact analysis in terms of maximal principal strains (left hand side) and computed distribution of energies in time (right hand side). Considered is the time interval up to the moment when the beam-hammer contact force drops approximately to zero. Within this time period the relevant damage of the beam takes place. It can be seen that for impact velocity of 2 m/s dominates mode-I fracture (bending failure). However, for impact velocity higher than 4 m/s dominates shear failure mode. Between impact velocities of 2 and 4 m/s there is a transition from bending to shear failure. Similar results were obtained by experimental investigations (Sukontasukkul and Mindess 2003). Note, that these "limit" impact velocities are valid only for the here investigated beam-hammer geometry and their mechanical properties. For other geometrical and mechanical properties these limit velocities would change, with the observed failure modes being the same.

From the computed distributions of energies (see Fig. 4), it can be seen that because of relatively high stiffness of the hammer, its deformation energy is negligible compared to the deformation energy of the beam. After approximately 0.30 ms the total kinetic energy of the hammer is transformed into deformational and kinetic energy of the beam. The figure shows that the total energy slightly decreases with time. For all loading rates the decrease is obvious only up to the point of transition of the total kinetic energy of the hammer into the beam (approximately up to $t = 0.30$ ms). The reason for this slight drop is the frictional energy between the beam and hammer, which is not included in the total energy plotted in Fig. 4. The smaller part of the energy loss is caused by numerical error. The energy curves show that the sum of deformational and kinetic energy is equal to the total energy (isothermal conditions), what confirms that dynamic equilibrium is fulfilled.

The predicted mid-span impact loads and reactions are as a function of time plotted in Fig. 5. Comparing the peak load for quasi-static load (see Fig. 3a) and impact load (Fig. 5a) it can be seen that the impact load is much higher than the quasi-static peak (failure) load. With increase of impact velocity the impact load increases. Compared to the impact load, the reaction forces are relatively small. They are activated after the beam is already significantly damaged and impact load already reduces almost to zero. This indicates that the load transfer takes place in a relatively small zone of the beam, close to impact zone, and that the impact load is almost entirely in equilibrium with inertia forces. With increase of loading velocity, the zone of the load transfer tends to be smaller, i.e., more localized (see Fig. 4). It can also be seen that just after the impact of the hammer, the reactions start to act in direction opposite to the impact load (positive reactions), however,

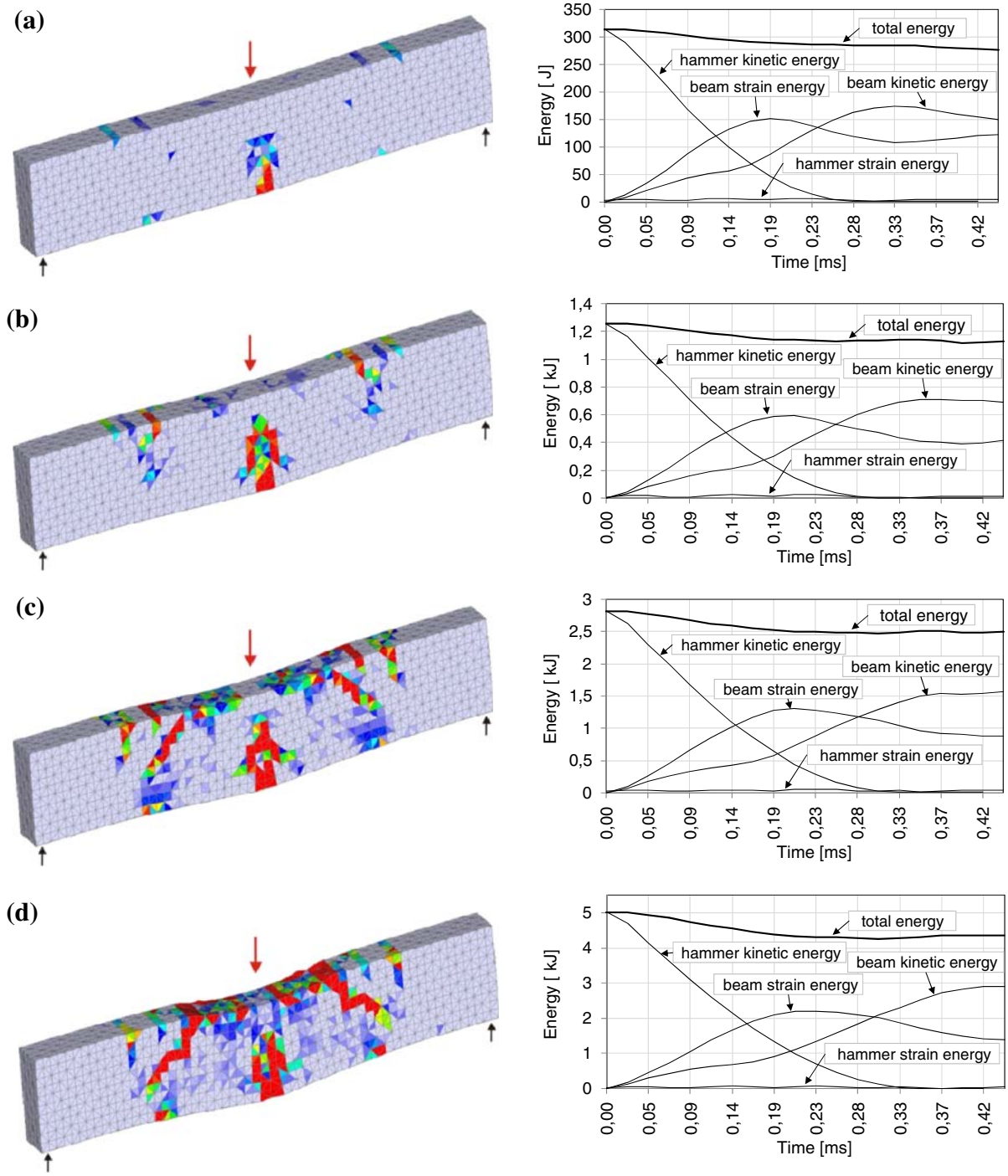

Fig. 4 Failure modes and energy balance for **a** Impact velocity of 2 m/s. **b** Impact velocity of 4 m/s. **c** Impact velocity of 6 m/s. **d** Impact velocity of 8 m/s

once the beam in the zone of impact is damaged, the left and the right part of the beam tend to be lifted up (negative reactions). The described mechanism can be illustrated by the plot of sequence of distribution of principal compressive stress waves shown in Fig. 6 for the case of impact velocity of 2 m/s. It can be seen that

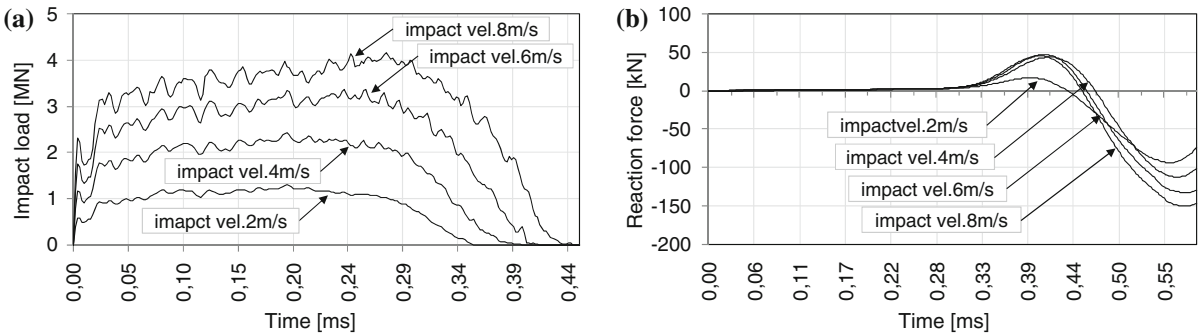

Fig. 5 Dynamic analysis **a** Impact load at the mid span versus time. **b** Support reaction versus time

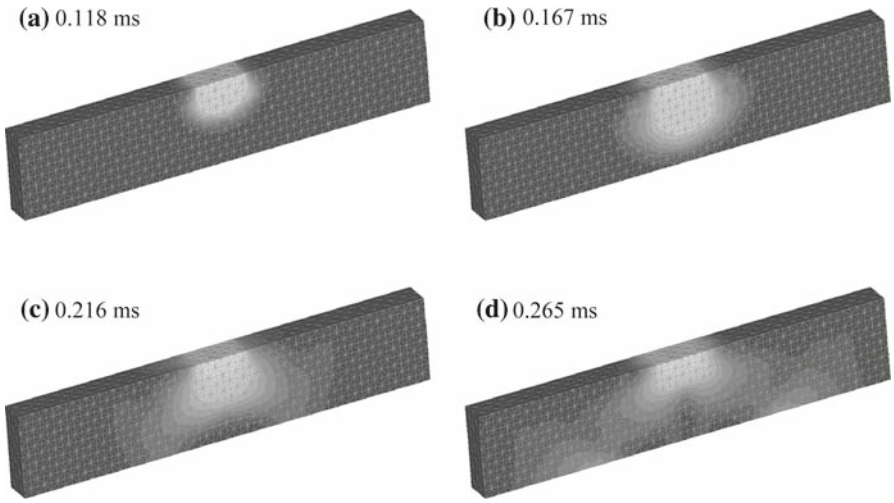

Fig. 6 Sequences of propagation of principal compressive stresses waves for impact velocity of 2 m/s (bending failure)

after the beam is damaged in the mid bottom region, the compressive wave propagates under an angle of approximately 35° (measured from the horizontal line) and reflects from the bottom free beam surface, under approximately the same angle, into the left and the right regions of the beam ends by pushing these parts of the beam into direction that is opposite to the load direction (negative reaction).

From the results shown in Fig. 6 it can be deduced that velocity of wave propagation through concrete is calculated correctly. Namely, for the used concrete the loading wave speed can be calculated from the material properties as $(E_c/\rho_c)^{0.5} = 3551$ m/s. Accounting for the beam geometry and the time predicted for the propagation of the loading wave from the top to the bottom of the beam (0.167 ms, Fig. 6b), it turns out the velocity of 3,593 m/s, what agrees well with the loading wave velocity for the used concrete (3,551 m/s).

In Fig. 7 are shown velocities of bending-crack tip as a function of time. They are obtained from the evaluation of numerical results. Plotted are absolute (Fig. 7a) and relative (Fig. 7b) velocities. The relative velocities are related to Rayleigh wave speed, which is for the used concrete $v_R = C_R(G_c/\rho_c)^{0.5} = 2{,}140$ m/s. Note, that the constant C_R depends on Poisson's ratio. For here used concrete it is equal to $C_R = 910$ (for crack velocity in m/s) and G_c is shear modulus of concrete. It is interesting to observe that after crack initiation there is almost linear increase in velocity of the crack tip up to the maximal velocity of approximately $0.55v_R$. This is in good agreement with theoretical prediction (Freund 1972a,b). From Fig. 7 can be seen that maximal crack speed only slightly increases with increase of impact velocity. According to theoretical solution for dynamic propagation of a single crack (Freund 1972a,b), for relative velocities greater than

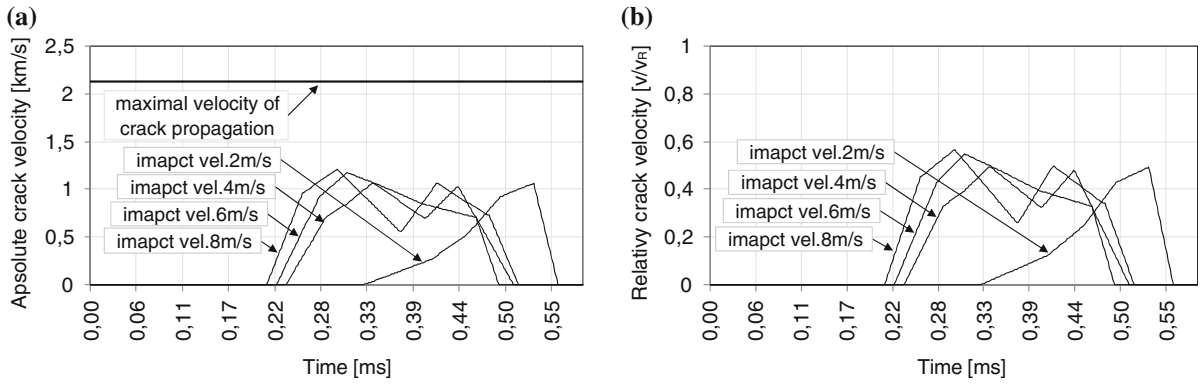

Fig. 7 Propagation of the bending crack as a function of time **a** Absolute velocity of the crack tip. **b** Relative velocity of the crack tip

0.5 crack branching of mode-I crack is possible. This is also confirmed by the results of the present study. Namely, Fig. 4b–d show that after reaching relative velocity of 0.5 bending crack tends to branch into two inclined cracks. Furthermore, the evaluation of results indicates that the acceleration at the crack tip is very high, i.e., for a few orders of magnitude higher than the gravity constant. How realistic are such values is difficult to say because it is well known that standard numerical integration scheme, such as used here, often leads to not accurate estimation of acceleration. Note, that because of relatively coarse FE mesh, the results related to the dynamic crack propagation can be considered only as qualitative. To get more detailed view into the dynamic crack propagation, numerical analysis should be carried out with finer discretization of the cracking zone.

The comparison between numerical and experimental results (Sukontasukkul and Mindess 2003), shows that the used numerical model is able to correctly capture the rate dependant failure mechanism of plain concrete beam. Similar as in the present study, the recent numerical studies (Ožbolt and Reinhardt 2005a,b); Ožbolt et al. 2006) show that for lower loading rates (bending failure) the rate sensitive response is controlled by local inertia forces at the crack tip. In the numerical analysis for this is accounted for by the rate dependent constitutive law of concrete. Furthermore, it is shown that for high and extremely high strain rates (shear failure mode), the structural inertia forces govern structural response and that the rate dependency at the constitutive level is much less important. The consequence is that the structural response is strongly dependent on the geometry of the structure. The same turns out to be the case in the present numerical study, what implies that, in contrary to lower loading rates, for higher loading rates bending reinforcement would have no or little effect on the failure mode that is of shear type.

5 Summary and conclusions

In the present paper the theoretical background, which is used in the numerical study of failure of plain concrete beam loaded by impact 3-point load is briefly discussed. The formulation of the problem is performed in the framework of continuum mechanics, following basic principles of irreversible thermodynamics. Based on the experimental and numerical results obtained in the study of rate dependent failure of plain concrete beam under impact load, the following can be concluded. (1) Loading rate has significant influence on the resistance and failure mode of plain concrete beam. The comparison between numerical and experimental results shows that the used numerical model is able to correctly predict the rate dependent failure of plain concrete beam. (2) For quasi-static load and relatively low impact load velocity, the beam fails in bending (mode-I fracture). With increase in impact velocity there is a transition of failure mode from dominant bending to dominant shear and the failure tends to be localized closer to impact zone. (3) For relatively low strain rates (mode-I fracture) local inertia forces at the micro-crack tip control the beam response. The rate dependent constitutive law for concrete can account for the rate dependent response. However, for higher loading rates the influence of loading rate on the beam response is mainly

controlled by structural inertia forces. Consequently, for higher loading rates the geometry (size) of the beam should have significant influence on the failure. (4) Because of the change of failure mode with increase in loading rate from bending to shear, in reinforced concrete beams loaded by higher loading rates bending reinforcement would be ineffective. Instead, the shear reinforcement is required to prevent failure. (5) Velocity of the bending crack tip increases almost linearly up to the peak value of approximately 0.55 Rayleigh wave speed. The maximal velocity only slightly increases with the increase of impact velocity. The analysis indicates branching of bending crack. (6) Further studies are needed to investigate dynamic crack propagation in more detail.

References

Banthia NP, Mindess S, Bentur A (1987) Impact behaviour of concrete beams. Mater Struct (MatOriaux et Constructions) 20:293–302

Bažant ZP, Oh BH (1983) Crack band theory for fracture of concrete. RILEM 93(16):155–177

Bažant ZP, Prat PC (1988) Microplane model for brittle-plastic material—parts I and II. J Eng Mech ASCE 114:1672–1702

Bažant ZP, Gettu R (1992) Rate effect and load relaxation in static fracture of concrete. ACI Mater J 89:456–468

Bažant ZP, Adley MD, Carol I, Jirasek M, Akers SA, Rohani B, Cargile JD, Caner FC (2000a) Large-strain generalization of microplane model for concrete and application. J Eng Mech ASCE 126(9):971–980

Bažant ZP, Caner FC, Adley MD, Akers SA (2000b) Fracturing rate effect and creep in microplane model for dynamics. J Eng Mech ASCE 126(9):962–970

Belytschko T, Liu WK, Moran M (2001) Nonlinear finite elements for continua and structures. Wiley, New Jersey

Bentur A, Mindess S, Banthia N (1987) The behaviour of concrete under impact loading: experimental procedures and method of analysis. Materials and Structures MatOriaux et Constructions 19- N $\sim$ 113

Carpenter NJ, Taylor JR, Katona MG (1991) Lagrange constraints for transient finite element surface contact. Int J Numer Methods Eng 32:103–128

Comite Euro-International Du Beton (CEB) (1988) Concrete structures under impact and impulsive loading. Syntesis report, Bulletin D'Information N_0 187

Crisfield MA (1991) Non-linear finite element analysis of solid and structures vol I. Wiley, NY

Curbach M. (1987) Festigkeitssteigerung von Beton bei hohen Belastungs-geschwindigkeiten. PhD. Thesis, Karlsruhe University, Germany

Dilger WH, Koch R, Kowalczyk R (1978) Ductility of plained and confined concrete under different strain rates. American Concrete Institute, Special publication, Detroit, Michigen

Freund LB (1972a) Crack propagation in an elastic solid subjected to general loading-I constant rate of extension. J Mech Phys Solids 20:129–140

Freund LB (1972b) Crack propagation in an elastic solid subjected to general loading-II non-uniform rate of extension. J Mech Phys Solids 20:141–152

Hutter M, Fuhrmann A (2007) Optimized continuous collision detection for deformable triangle meshes, research grant KF0157401SS5 in the PRO INNO II program, Germany

Krausz AS, Krausz K (1988) Fracture kinetics of crack growth. Kluwer, Dordrecht

Ožbolt J, Bažant ZP (1996) Numerical smeared fracture analysis: nonlocal microcrack interaction approach. Int J Numer Methods Eng 39:635–661

Ožbolt J, Reinhardt HW (2001) Three-dimensional finite element model for creep-cracking interaction of concrete. In: Ulm, Bažant, Wittmann (eds) Proceedings of the sixth international conference CONCREEP-6, pp 221–228

Ožbolt J, Li Y, Kožar I (2001) Microplane model for concrete with relaxed kinematic constraint. Int J Solid Struct 38:2683–2711

Ožbolt J, Reinhardt HW (2005a) Dehnungsgeschwindigkeitsabhängiger Bruch eines Kragträgers aus Beton. Bauingenieur Springer VDI Band 80:283–290

Ožbolt J, Reinhardt HW (2005b) Rate dependent fracture of notched plain concrete beams. In: Pijaudier-Cabot, Gerard, Acker (eds) Proceedings of the 7th international conference CONCREEP-7, pp 57–62

Ožbolt J, Rah KK, Mestrović D (2006) Influence of loading rate on concrete cone failure. Int J Fract 139:239–252

Reinhardt HW (1982) Concrete under impact loading tensile strength and bond. Heron 27:3

Saatci S, Vecchio JV (2009) Effect of shear mechanisms on impact behavior of reinforced concrete beams. ACI Struct J 106(1):78–86

Sukontasukkul P, Mindess S (2003) The shear fracture of concrete under impact loading using end confined beams. Mater Struct (Matdriaux et Constructions) 36:372–378

Weerheijm J (1992) Concrete under impact tensile loading and lateral compression. Dissertation, TU Delft

Wriggers P (2002) Computational Contact Mechanics, John Wiley & Sons Ltd, The Atrium, Southern Gate, Chichester, West Sussex PO19 8SQ

Zienkiewicz OC, Taylor RL, Zhu JZ (2005) The finite element method—its basis and fundamentals, 6th edn. Elsevier Butterworth-Heinemann, Massachusetts